npj | computational materials

www.nature.com/npjcompumats

ARTICLE OPEN

Check for updates

Vibrationally resolved optical excitations of the nitrogen-vacancy center in diamond

Yu Jin[1], Marco Govoni[2,3]✉ and Giulia Galli[1,2,3]✉

A comprehensive description of the optical cycle of spin defects in solids requires the understanding of the electronic and atomistic structure of states with different spin multiplicity, including singlet states which are particularly challenging from a theoretical standpoint. We present a general framework, based on spin-flip time-dependent density function theory, to determine the excited state potential energy surfaces of the many-body singlet states of spin defects; we then predict the vibrationally resolved absorption spectrum between singlet shelving states of a prototypical defect, the nitrogen-vacancy center in diamond. Our results, which are in very good agreement with experiments, provide an interpretation of the measured spectra and reveal the key role of specific phonons in determining absorption processes, and the notable influence of non-adiabatic interactions. The insights gained from our calculations may be useful in defining strategies to improve infrared-absorption-based magnetometry and optical pumping schemes. The theoretical framework developed here is general and applicable to a variety of other spin defects and materials.

npj Computational Materials (2022)8:238 ; https://doi.org/10.1038/s41524-022-00928-y

INTRODUCTION

Spin defects in semiconductors and insulators have attracted considerable attention in the last decade, as promising platforms to realize quantum technologies[1]. For example, it has been shown that simple point defects such as the negatively charged nitrogen-vacancy (NV^-) in diamond[2] may be used as quantum bits (qubits), where the qubit initialization and readout is realized through an optical spin-polarization cycle between the triplet ground state, a triplet excited state and two shelving singlet states[3–6]. The ability to initialize and readout the NV^- center in diamond has led to numerous proposals for quantum technology applications[7,8], including quantum sensing[9,10] and communication[11], and possibly quantum computation[12,13].

While the optical and magnetic properties of the triplet ground and the first triplet excited state of the NV^- center have been extensively investigated using density functional theory (DFT)[8,14–20], robust first-principles predictions of the properties of the singlet shelving states are not yet available. The reason is two-fold: the description of the electronic structure of these singlet states requires a higher level of theory than DFT to account for their strongly correlated (multiconfigurational) nature; in addition, the determination of their atomistic structure requires techniques capable of optimizing complex excited state potential energy surfaces (PESs), beyond DFT with constrained occupations (ΔSCF). Important progress has been reported in using high level theories to investigate the electronic structure of the shelving singlets of the NV^- center, at fixed geometries; these theories include many-body perturbation theory (*GW* and the solution of the Bethe–Salpeter Equation (BSE)[21]), quantum chemistry methods, e.g., complete active space self-consistent field (CASSCF)[22], the diagonalization of effective Hamiltonian derived within the constrained random-phase approximation (CRPA)[23], and a quantum defect embedding theory (QDET)[24–29]. However, all these approaches have been limited to the evaluation of vertical excitation energies (VEEs) at given geometries; the PESs of the singlet states and their vibrationally resolved optical spectra have not been predicted from first principles. In a pioneering work, Thiering and Gali[6] investigated optical transitions and inter-system crossings involving singlet states, based on a model Hamiltonian parameterized by DFT calculations. However, they included parameters fitted to experiments, e.g., the energy spacing between the singlet states, and overall they obtained a fair agreement between experiments and computed absorption spectra.

With the goal of providing a comprehensive description of the optical cycle of the NV^- center, we investigate the electronic and atomistic structure of the singlet states involved in the optical cycle. We present a general framework based on the implementation of spin-flip time-dependent density function theory (TDDFT)[30–36] using a planewave basis set, which allows for a robust determination of the excited states PESs. We use both the semi-local functional by Perdew, Burke and Ernzerhof (PBE)[37] and the dielectric-dependent hybrid (DDH) functional[38] and we evaluate analytical forces acting on the nuclei[39,40]. By computing many-body electronic states, equilibrium geometries, and phonons of the singlet states, we successfully predict the infrared vibrationally resolved absorption spectrum[41] between singlet shelving states using the Huang–Rhys (HR) theory[17,19,20,42]. Our results, which are in very good agreement with experiments, provide an interpretation of the measured spectra and reveal the key role of specific phonons in determining absorption processes, and the notable influence of non-adiabatic interactions. The insights gained from our calculations may be useful in defining strategies to improve infrared-absorption-based magnetometry[43–46] and optical pumping schemes. The theoretical framework developed and used here is general and applicable to a variety of other spin defects and materials.

The rest of the paper is organized as follows. We first present our electronic structure calculations of the many-body electronic states of the NV^- center at a fixed geometry, followed by the

[1]Department of Chemistry, University of Chicago, Chicago, IL 60637, USA. [2]Pritzker School of Molecular Engineering, University of Chicago, Chicago, IL 60637, USA. [3]Materials Science Division and Center for Molecular Engineering, Argonne National Laboratory, Lemont, IL 60439, USA. ✉email: mgovoni@anl.gov; gagalli@uchicago.edu

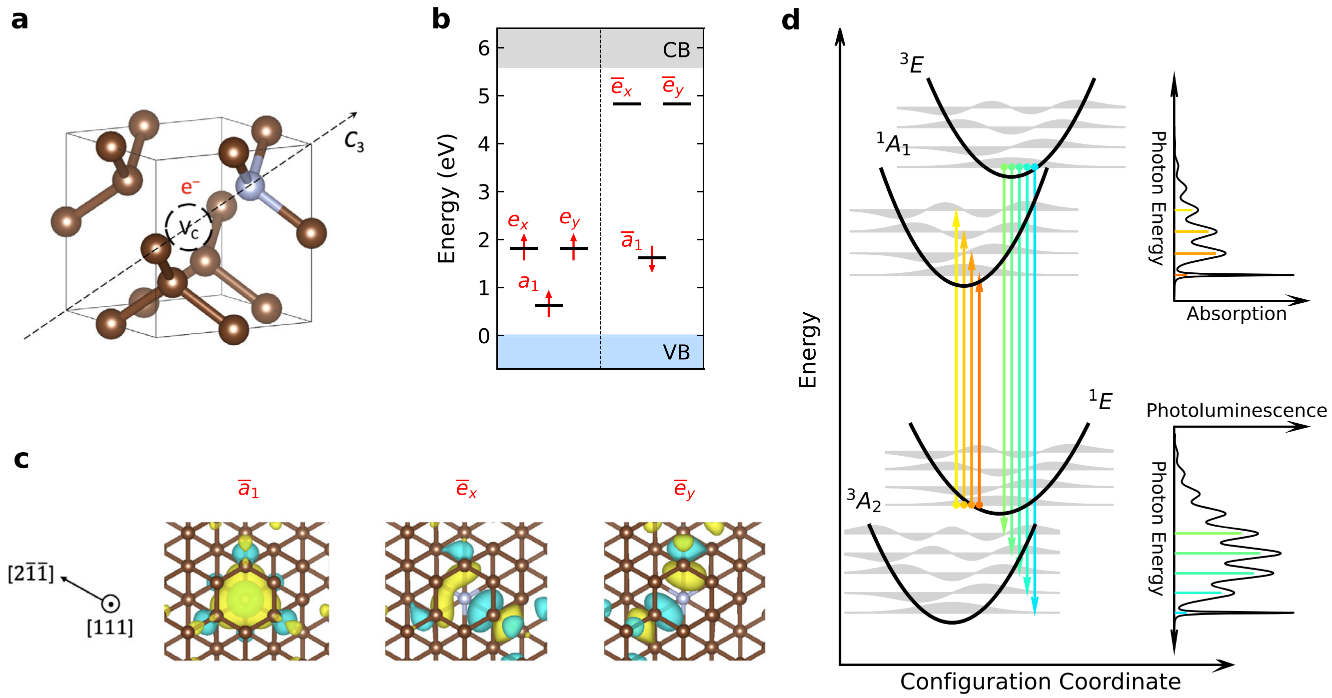

Fig. 1 Description of the NV$^-$ center in diamond. a Ball and stick representation, with the vacancy depicted as a circle in the middle of the diamond cage, and the carbon and nitrogen atoms represented by brown and gray spheres, respectively. The defect has C_{3v} symmetry, with a threefold rotation axis (C_3) parallel to the $\langle 111 \rangle$ axis of diamond. **b** Position of the single-particle defect levels in the band gap of diamond, labeled according to the irreducible representation of the C_{3v} group, and computed by spin unrestricted density functional theory calculations with the DDH hybrid functional[38]. **c** Isosurfaces of the square moduli of the single-particle orbitals associated to the defect levels. The color (yellow/light blue) represents the sign (+/−) of the orbital. **d** Schematic diagram illustrating optical processes leading to the photoluminescence (PL) of the $^3E \rightarrow {}^3A_2$ transition and the absorption of the $^1E \rightarrow {}^1A_1$ transition (see text). For ease of graphical representation, the potential energy surfaces (PESs) are shown as parabolas. Vibrational wavefunctions are schematically shown in gray. Colored arrows represent optical transitions at 0 K. PL and absorption line shapes containing sharp zero-phonon lines and broad phonon side bands are shown as insets.

determination of their PESs. We then discuss electron–phonon coupling and finally present the vibrationally resolved optical absorption spectrum of the spin-defect. We close the paper with a discussion and summary of all the results.

RESULTS

Many-body electronic states and vertical excitation energies

As well known, the NV$^-$ center in diamond is composed of a nitrogen impurity and an adjacent carbon vacancy (V_C) (see Fig. 1). The defect has C_{3v} symmetry, with three orbitals within the band gap of diamond (one a_1 and two-fold-degenerate e orbitals), localized on three carbon sites in the vicinity of V_C. Hereafter, we denote the spin up (down) defect orbitals as a_1, e_x, e_y ($\bar{a}_1$, $\bar{e}_x$, $\bar{e}_y$). The low-lying many-body triplet states are denoted as $^3A_2$ (ground state) and ^3E and the singlet states as ^1E and $^1A_1$[47,48]. In the $m_s = 1$ sublevel of the $^3A_2$ ground state, a_1, e_x, e_y and $\bar{a}_1$ are occupied by four electrons, while $\bar{e}_x$, $\bar{e}_y$ are empty, and its electronic configuration is represented by the Slater determinant $|\bar{e}_x\bar{e}_y\rangle$ in the hole notation. Similarly, phonon modes of the NV$^-$ center are also labeled as a_1, a_2 and e type according to the C_{3v} point group.

We computed the VEEs of the triplet ^3E and singlet states ^1E and $^1A_1$ with respect to the $^3A_2$ ground state using TDDFT and the semi-local functional PBE (TDDFT@PBE) and hybrid functional DDH (TDDFT@DDH), with the aim of establishing the accuracy of the chosen electronic structure methods, before proceeding with structural optimizations. Our results are shown in Fig. 2, together with those of other calculations[21–23,29] and inferred experimental values[49–52]. Irrespective of the functional, TDDFT correctly predicts the ordering of singlet and triplet excited states. However, at the PBE level of theory, TDDFT underestimates the energies of the ^3E and the $^1A_1$ states with respect to the $^3A_2$ ground state compared to experiment; the agreement is improved when using the hybrid functional DDH, where the inclusion of a portion of Hartree–Fock exact exchange interaction provides a more accurate description of excitonic effects. The latter yields the energy of ^3E in good accord with *GW*-BSE results[21], but those of the ^1E and $^1A_1$ states differ, likely due to the fact that, in contrast to *GW*-BSE, in TDDFT an approximate non-collinear spin-flip kernel is introduced to describe spin-flip excitations.

In spite of the correct ordering, the VEEs obtained at the TDDFT@DDH level of theory are an overestimate, especially for singlets, relative to the experimental values. To understand the origin of this discrepancy we compared the many-body wavefunctions obtained with TDDFT with those computed with QDET[29]; the latter includes double and higher-order excitations from the $^3A_2$ ground state which is represented by the Slater determinant $|\bar{e}_x\bar{e}_y\rangle$ in our spin unrestricted DFT calculations. These excitations are not included in the TDDFT calculations presented here (and also in the *GW*-BSE calculations of ref. [21]). In QDET, the defect states are described by an effective many-body Hamiltonian diagonalized exactly by full configuration interaction (CI) and hence the many-body wavefunction contains higher-order excitations. The Hamiltonian includes the interaction of the defect and the solid where it is embedded through an effective dielectric screening. The many-body electronic wavefunctions $|\Phi_i\rangle$ are written as linear combinations of Slater determinants $|\Psi_n\rangle$:

$$|\Phi_i\rangle = \sum_n c_n^i |\Psi_n\rangle, \tag{1}$$

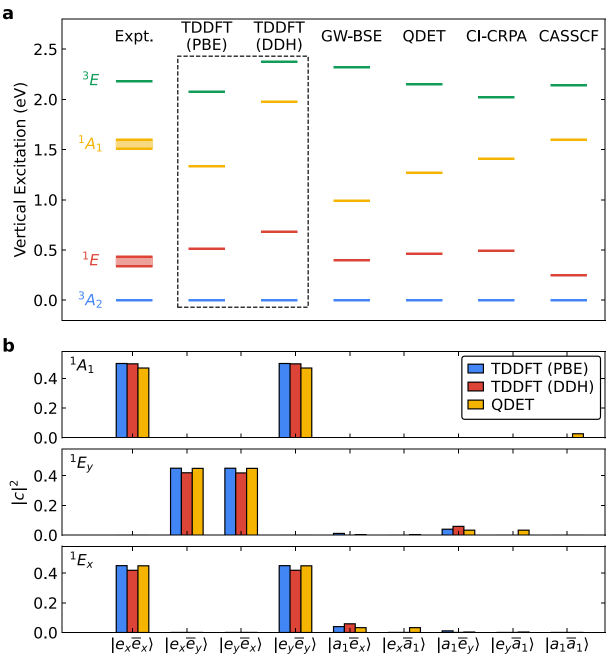

Fig. 2 Many-body electronic states of the NV$^-$ center in diamond. **a** Vertical excitation energies (VEEs) of the low-lying many-body electronic states at the ground state geometry, computed using time-dependent density functional theory (TDDFT), and using PBE and DDH functionals are shown in the rectangle. Experimentally inferred VEE of the ^3E state and zero-phonon absorption energies of the $^1A_1$ and ^1E states are from refs. [49–52]. We also report theoretical results obtained using *GW* and the Bethe–Salpeter Equation (BSE)[21], quantum defect embedding theory (QDET)[29], results obtained from the constrained random-phase approximation solved by configuration interaction (CI-CRPA)[23], and quantum chemistry results for clusters from complete active space self-consistent field (CASSCF)[22] calculations. **b** Contribution of Slater determinants of single excitation ($|e_x\bar{e}_x\rangle$, $|e_x\bar{e}_y\rangle$, $|e_y\bar{e}_x\rangle$, $|e_y\bar{e}_y\rangle$, $|a_1\bar{e}_x\rangle$ and $|a_1\bar{e}_x\rangle$) and double excitation ($|e_x\bar{a}_1\rangle$, $|e_y\bar{a}_1\rangle$ and $|a_1\bar{a}_1\rangle$) with respect to the $^3A_2$ ground state represented by Slater determinant $|\bar{e}_x\bar{e}_y\rangle$ to the wavefunction of the singlet states, as obtained from TDDFT and QDET[29] calculations. Slater determinants are denoted in the hole notation, and their contributions to the total wavefunction are given in terms of the coefficients defined in Eq. (1) (see text). Both TDDFT and QDET calculations are performed at the geometry of the $^3A_2$ ground state with C_{3v} symmetry.

where $|c_n^i|^2$ represents the contribution of the *n*th Slater determinant to the *i*th many-body electronic wavefunction. The Slater determinants with contributions to the total wavefunction larger than 1% are reported in Fig. 2 and in Supplementary Table 2 for the three singlet states, for both QDET and spin-flip TDDFT calculations. Note that we use $^1A_1^{(0)}$, $^1E_x^{(0)}$ and $^1E_y^{(0)}$ to denote states with C_{3v} symmetry, and in the section "Potential energy surfaces of electronic excited states", we use $^1A_1$ and ^1E to denote singlet states in geometrical configurations where the C_{3v} symmetry is not preserved. As shown in Fig. 2, the major contributions to the many-body electronic states $^1A_1^{(0)}$, $^1E_x^{(0)}$ and $^1E_y^{(0)}$ come from linear combinations of Slater determinants with only single excitations, which are accounted for when using spin-flip TDDFT, and yield contributions similar to QDET. However, QDET calculations show an additional, non-negligible (~3%) contribution to the total wavefunction coming from determinants containing double excitations that cannot be described by TDDFT: $|a_1\bar{a}_1\rangle$, $|e_x\bar{a}_1\rangle$, and $|e_y\bar{a}_1\rangle$, for electronic states $^1A_1^{(0)}$, $^1E_x^{(0)}$ and $^1E_y^{(0)}$, respectively.

By adding the contributions of double excitations to our spin-flip TDDFT results, using perturbation theory, we find that the energies of the $^1A_1$ and ^1E states decrease by 0.2~0.3 eV, resulting in a better agreement with experiments and QDET values (see Supplementary Note 2). Hence we conclude that the absence of double excitations in the TDDFT description leads to a moderate overestimate of the energy of singlets relative to QDET results. In summary, TDDFT calculations yield results for VEEs in good (albeit not perfect) agreement with those of QDET and experiments, and account for the majority of excitations entering the many-body wavefunctions of the NV$^-$ center, giving us confidence that the geometries of singlet manifolds obtained using spin-flip TDDFT and all single excitations are reliable.

Potential energy surfaces of electronic excited states

Having established the accuracy of TDDFT in describing VEEs, we proceed to optimize the geometry of the system in each excited state using TDDFT forces acting on nuclei. The PESs of singlets are computed by carrying out calculations on two specific geometrical paths, described by collective variables (CVs) defined below. We then define an effective Hamiltonian for ionic and electronic degrees of freedom, including electron–phonon interaction, and we investigate the non-adiabatic coupling between many-body electronic states and lattice vibrations.

We start by describing the optimized geometrical configurations of electronic excited states, quantified in terms of mass-weighted atomic displacements and Franck–Condon shifts (see Supplementary Note 3). We find that the optimized geometry of the triplet excited state ^3E exhibits a significant displacement of ~0.6 amu$^{0.5}$ Å and a Franck–Condon shift of ~200 meV, relative to the geometry of the ground state. These results obtained with TDDFT forces are consistent with our previous study, where geometry optimization of the triplet excited state was obtained with ΔSCF, and results were validated against photoluminescence (PL) measurements[20]. The singlet states cannot be simulated with ΔSCF. Hence, we optimize their geometries using forces computed with spin-flip TDDFT and a planewave basis set. The two singlet states have rather different optimized configurations: that of the $^1A_1$ state is similar to the optimized geometry of the ground state (with a negligible atomic displacement of ~0.1 amu$^{0.5}$ Å and a Franck–Condon shift of 17 meV), while the ^1E state exhibits a displacement of ~0.4 amu$^{0.5}$ Å and a Franck–Condon shift of 60~100 meV.

We then computed the variation of the distances (Δ*d*) of the three carbon atoms close to V_C in the excited states (d_{ES}), relative to the ground state (d_{GS}); these are shown in Fig. 3. We find an asymmetric displacement pattern for the ^1E singlet, suggesting the existence of three equivalent equilibrium geometries, compatible with the C_{3v} symmetry of the defect, which we characterized in terms of two CVs, Q_α and Q_β. Q_β defines a direction connecting two of the three geometrical configurations, and Q_α is perpendicular to Q_β. The three geometrical configurations form an equilateral triangle on the plane defined by Q_α and Q_β. The minimum of the $^1A_1$ singlet PES on the plane of Q_α and Q_β is located at the center of the triangle (defined by $Q_\alpha = 0$, $Q_\beta = 0$), and is very close to the actual minimum of the $^1A_1$ singlet with a negligible displacement of 0.08 amu$^{0.5}$ Å. Using the CVs Q_α and Q_β we computed the total energies of the singlet many-body states along two paths, using TDDFT@PBE: path 1, parallel to Q_α, with $Q_\beta = 0$, which connects one of the local minima and the center of the triangle; path 2, parallel to Q_β, with $Q_\alpha = 0$, and crossing the triangle center (see Supplementary Fig. 1). For values of Q_α and Q_β different from zero, and along both paths 1 and 2, we find that the wavefunctions of the $^1A_1$ and ^1E singlets, as computed using TDDFT, are linear combinations of the states with C_{3v} symmetry previously identified as $^1A_1^{(0)}$, $^1E_x^{(0)}$ and $^1E_y^{(0)}$. For the $^1A_1$ singlet, the wavefunction is given by a linear combination of the $^1A_1^{(0)}$ component, mixed with a small amount (<10%) of the $^1E_x^{(0)}$ component along path 1 (or $^1E_y^{(0)}$ component along path 2). The

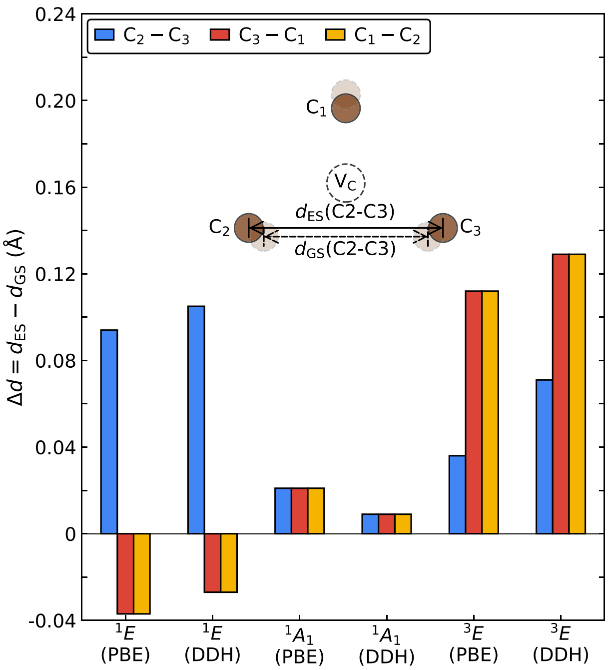

Fig. 3 Geometrical configurations of many-body states of the NV$^-$ center in diamond. Differences of the distances between the three carbon atoms (C_1, C_2 and C_3) around the vacancy site (V_C), as obtained in the excited states (ES) and ground state (GS): $\Delta d = d_{ES} - d_{GS}$. The differences are reported for the ^1E, $^1A_1$ and ^3E ESs and are computed using TDDFT with PBE or DDH functionals. Note that $\Delta d(C_1 - C_2)$, $\Delta d(C_2 - C_3)$ and $\Delta d(C_3 - C_1)$ for the ^3E state differ, due to the coupling of the electronic state to both a_1 and e type phonon modes (see text). For the $^1A_1$ state, $\Delta d(C_1 - C_2)$, $\Delta d(C_2 - C_3)$ and $\Delta d(C_3 - C_1)$ are instead all equal to ~0.02 Å, implying that in this case the equilibrium geometry preserves the C_{3v} symmetry and is close to that of the $^3A_2$ ground state. The differences $\Delta d(C_1 - C_2)$, $\Delta d(C_2 - C_3)$ and $\Delta d(C_3 - C_1)$ of the ^1E state differ, due to a significant coupling with e type phonon modes, leading to symmetry breaking.

magnitude of the mixing between states with C_{3v} symmetry increases as the absolute value of Q_α and Q_β increases. While the wavefunction of the ^1E singlet on path 1 can still be approximately identified as the so called "pure" state $^1E_x^{(0)}$ or $^1E_y^{(0)}$, on path 2, the wavefunction is given by a linear combination with approximately equal weights of the $^1E_x^{(0)}$ and $^1E_y^{(0)}$ components. The mixing of components found in our calculations points at the non-adiabatic coupling occurring in the system, which requires further analysis, as we discuss next.

To analyze in detail the PESs of the singlet states, we define an effective Hamiltonian that includes electron–phonon (non-adiabatic) coupling[6,53], and where the nuclei are represented in terms of the CVs defined above, and the electrons in the basis of the three singlet states $^1A_1^{(0)}$, $^1E_x^{(0)}$ and $^1E_y^{(0)}$ at $Q_\alpha = 0$ and $Q_\beta = 0$:

$$\hat{H} = \hat{H}_e + \hat{H}_{ph} + \hat{H}_{e-ph}. \tag{2}$$

Here $\hat{H}_e = \sum_i E_i \hat{c}_i^\dagger \hat{c}_i$ is the electronic Hamiltonian, and $\hat{c}_i^\dagger$ ($\hat{c}_i$) is the creation (annihilation) operator of the ith many-body electronic state with $E_i = (\Lambda, 0, 0)$ for $|\Phi_i\rangle = (|^1A_1^{(0)}\rangle, |^1E_x^{(0)}\rangle, |^1E_y^{(0)}\rangle)$; $\Lambda = 821$ meV is the energy gap between the $^1A_1^{(0)}$ and degenerate $^1E_x^{(0)}$ and $^1E_y^{(0)}$ electronic states obtained with TDDFT@PBE. $\hat{H}_{ph} = \sum_{\lambda=\alpha,\beta} \hbar\omega_e (\hat{b}_\lambda^\dagger \hat{b}_\lambda + \frac{1}{2})$ is the Hamiltonian of the two-dimensional harmonic oscillator written in terms of Q_α and Q_β, with an effective phonon energy of $\hbar\omega_e$, and $\hat{b}_\lambda^\dagger$ ($\hat{b}_\lambda$) is the creation (annihilation) operator of phonon λ. The electron–phonon coupling term reads

$$\hat{H}_{e-ph} = \sum_{ij} \sum_{\lambda=\alpha,\beta} g_{ij,\lambda} \hat{c}_i^\dagger \hat{c}_j \left(\hat{b}_\lambda^\dagger + \hat{b}_\lambda\right), \tag{3}$$

where $g_{ij,\lambda}$ is the linear electron–phonon coupling strength between electronic state i, j and phonon mode λ. Details on our first-principles calculation of the electron–phonon coupling strength and the analysis of the Hamiltonian of equation (2) in terms of pseudo- and dynamical Jahn–Teller effects are given in Supplementary Note 4.

To obtain the adiabatic PESs of the singlet states we write $\hat{b}_\lambda = \sqrt{\frac{\omega_e}{2\hbar}}(\hat{Q}_\lambda + \frac{i}{\omega_e}\hat{\Pi}_\lambda)$, where $\hat{\Pi}_\lambda$ is the momentum operator. Treating Q_λ and Π_λ as classical coordinates allows us to separate the kinetic and potential energy terms in the Hamiltonian, and hence to obtain the adiabatic PESs, which are displayed in Fig. 4c–e. We obtained the parameters of the Hamiltonian, including the effective phonon energy $\hbar\omega_e = 63$ meV and the electron–phonon coupling strength $g_{ij,\lambda}$, by fitting the PESs obtained with the Hamiltonian equation (2) to our first-principles calculations, without introducing any empirical parameters (see Supplementary Fig. 2). The lower branch of the PES of the ^1E singlet exhibits a "tricorn Mexican hat" shape with three minima and three saddle points, and is connected to the higher branch through a cusp. The PES of the $^1A_1$ singlet slightly deviates from a perfect two-dimensional paraboloid, and the anharmonicity is most apparent along the path connecting its minimum to the minima on the lower branch of the ^1E state PES.

By solving the effective Hamiltonian equation (2) considering quantized vibrations, instead of classical coordinates, we obtain the vibronic levels of the two singlet states, as shown in Fig. 4b. We find that the vibronic levels with major electronic contribution from the $^1A_1$ singlet state are well approximated by harmonic vibrational levels, being almost equidistant with an energy gap of ~80 meV. The energy gap is 17 meV higher than the energy of the effective phonon defined in Eq. (2), as a result of the non-adiabatic coupling. Non-adiabatic coupling also results in noticeable anharmonicity: the energy difference between adjacent vibronic levels with major contribution coming from $^1A_1$ decreases as the quantum number increases. On the other hand, the vibronic levels with major electronic contribution from the ^1E singlet state are substantially different from those of a quantum harmonic oscillator. Our calculations identify an $\widetilde{A}_1$ state 10 meV above the vibronic ground state ($^1\widetilde{E}$), which likely corresponds to the state detected experimentally at about 14–16 meV[3,54–56], as has been discussed in ref. [6]. Such state is not accessible under equilibrium conditions but can be reached when the crystal is under uniaxial stress. We also find degenerate $\widetilde{E}$ vibronic levels at 49.3 meV above the vibronic ground state; the transition into these states might be the origin of the phonon side band at 42.6 meV observed in the low-temperature experimental PL spectrum of the $^1A_1 \rightarrow {}^1E$ transition[50].

Finally we note that, unlike the $^1E \rightarrow {}^1A_1$ absorption line shape, the calculation of the $^1A_1 \rightarrow {}^1E$ PL line shape would require an evaluation of all the phonon modes of the ^1E state, whose PES is strongly anharmonic, as well as an explicit treatment of the non-adiabatic coupling including all phonon modes[19]. Although in principle possible, these calculations are beyond the scope of the present work.

Optical spectra

We now turn to the discussion of our calculations of the vibrationally resolved absorption spectrum for the transition between singlet states, which we compare with experiments and with the PL spectrum for the transition between triplet states.

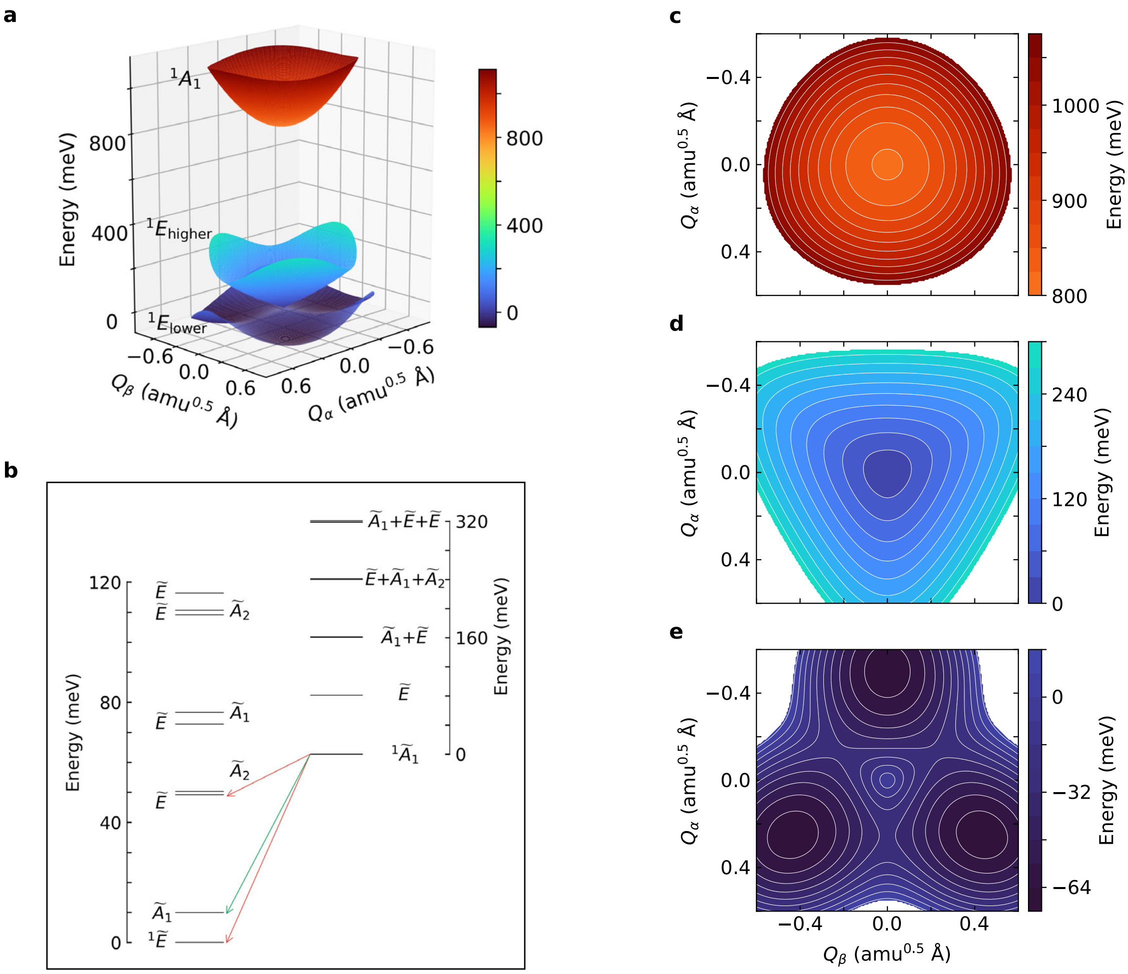

Fig. 4 Potential energy surfaces (PESs) and vibronic energy levels of the many-body electronic states of the NV$^-$ center in diamond. **a** Adiabatic PESs of the lower and higher branches of the ^1E and $^1A_1$ states. The Q_α, Q_β configuration coordinates (see text) represent the collective motion of effective phonon modes with e symmetry. Contour plots of the PESs are shown in **c**–**e**. The PES of the ^1E lower branch (**e**) has the "tricorn Mexican hat" shape with three minima and three saddle points, and is connected to the higher branch (**d**) through a cusp. The PES of the $^1A_1$ singlet (**c**) slightly deviates from a perfect two-dimensional paraboloid. **b** The vibronic levels of the ^1E (left) and $^1A_1$ (right) states, whose vibronic ground states are labeled as $^1\widetilde{E}$ and $^1\widetilde{A}_1$, respectively. The energy differences of vibronic levels of the $^1A_1$ from bottom to top are found to be 80.8, 79.7, 78.8, and 77.3 meV, respectively. The selection rules for the photoluminescence (PL) are indicated as arrows: red arrows represent the optically active $^1\widetilde{A}_1 \rightarrow {}^1\widetilde{E}$ transition resulting in the zero-phonon line (ZPL) and the $^1\widetilde{A}_1 \rightarrow \widetilde{E}$ transition resulting in the phonon side band shifted by 49.3 meV from the ZPL; the green arrow represents the $^1\widetilde{A}_1 \rightarrow \widetilde{A}_1$ transition, shifted by 10.0 meV from the ZPL, and can be activated by uniaxial stress. In the plot, the values of the ZPL and side bands are not given on the same energy scale for clarity.

Having computed the forces acting on nuclei with spin-flip TDDFT and all phonon modes in the $^1A_1$ state, we calculated the vibrationally resolved absorption spectrum of the transition between the ^1E and $^1A_1$ singlets using the HR theory. At $T \sim 0$ K, transitions occur from the lowest vibronic level of the ^1E state whose vibronic wavefunction is localized in the local minimum of the PES, into vibronic levels of the $^1A_1$ singlet state; these levels are all well approximated by harmonic vibrational levels; hence the use of the HR theory is justified.

Our results are compared with experiment[41] in Fig. 5. The agreement is very good (see Supplementary Note 5 for a comparison of results obtained using different functionals), and we successfully predict the main peak at 73 meV and the sharp peak at 170 meV. Note that the energy of the main peak is 7 meV smaller than the distance between vibronic levels of the $^1A_1$ state obtained from the effective Hamiltonian equation (2), pointing at the importance of including all phonon modes in the calculation of optical spectra. The level of agreement obtained here indicates that our first-principles calculations based on spin-flip TDDFT provides an improved description of the atomic geometries and vibrational properties of the singlet states. Such properties are not accessible in ΔSCF and hence their calculations require the implementation of TDDFT forces. In addition, we emphasize the importance of including the anharmonicity of the PES of the $^1A_1$ singlet in the calculation of the HR factors and spectral functions (see Supplementary Note 7).

Note that the phonon side band of the absorption line shape for the $^1E \rightarrow {}^1A_1$ transition decays much faster compared with that of the PL spectrum for the $^3E \rightarrow {}^3A_2$ transition (shown in Fig. 5a for comparison). Indeed, the computed Debye–Waller factor (the ratio of the zero-phonon line (ZPL) relative to the entire line shape) of the $^1E \rightarrow {}^1A_1$ absorption line shape is 34%, in good agreement with the inferred experimental value of ~40%[41], and is 10 times larger than that of the $^3E \rightarrow {}^3A_2$ PL line shape. The large Debye–Waller factor suggests that the ZPL is more absorptive than the phonon side band and hence better suited for infrared-

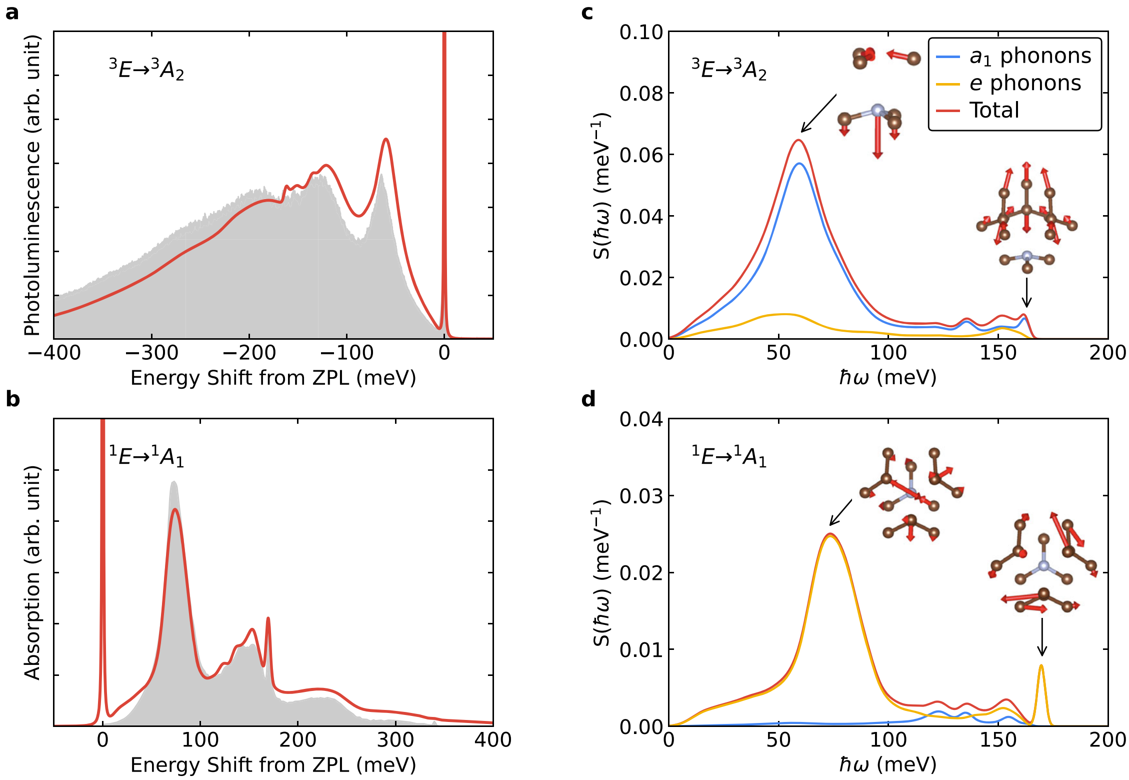

Fig. 5 Optical spectra and spectral densities. **a** Photoluminescence (PL) line shapes of the $^3E \rightarrow ^3A_2$ transition and **b** absorption line shapes of the $^1E \rightarrow ^1A_1$ transition. Red lines are theoretical results while the gray area represents experimental spectra from refs. [17,41]. Spectral densities $S(\hbar\omega)$ of the $^3E \rightarrow ^3A_2$ (**c**) and the $^1E \rightarrow ^1A_1$ transitions (**d**). Contributions from a_1 and e type phonon modes are shown as blue and yellow lines, respectively. The quasi-local (local) a_1 mode at 60 meV (162 meV) of the $^3A_2$ state that strongly couples with the $^3E \rightarrow ^3A_2$ transition is shown in the inset of **c**. The quasi-local (local) e mode at 73 meV (170 meV) of the $^1A_1$ state that strongly couples with the $^1E \rightarrow ^1A_1$ transition is shown in the inset of **d**. Results reported here are based on phonons computed at the PBE level of theory and optimized geometries computed at the DDH level of theory, and are extrapolated to the dilute limit, approximated by a $(12 \times 12 \times 12)$ supercell with 13,824 atomic sites. A comparison of results obtained using different functionals is given in Supplementary Note 5.

absorption-based magnetometry measurements than the phonon side band wavelengths[41].

It is interesting to analyze the main differences between singlet absorption and triplet PL spectra in terms of the spectral density of the electron–phonon coupling in the two cases, $S(\hbar\omega)$, as shown in Fig. 5c, d. The main contribution to the $S(\hbar\omega)$ of the $^1E \rightarrow ^1A_1$ transition comes from the coupling of the electronic states with e type phonon modes; instead the main contribution in the case of the $^3E \rightarrow ^3A_2$ transition originates from the coupling with a_1 type phonon modes. In more detail, we find that $S(\hbar\omega)$ of the $^1E \rightarrow ^1A_1$ transition exhibits a broad peak at 73 meV and a sharp peak at 170 meV, resulting from the coupling of the electronic states with a quasi-local and a local e type phonon mode, displayed in the inset of Fig. 5d. The 170 meV e type local mode exists only in the $^1A_1$ state and has an energy higher than that of the optical phonons of diamond. It couples weakly to the vibrations of the diamond lattice, resulting in a sharp peak in both $S(\hbar\omega)$ and the adsorption spectrum. The $S(\hbar\omega)$ of the $^1E \rightarrow ^1A_1$ transition is generally shifted to higher energy relative to that of the $^3E \rightarrow ^3A_2$ transition, originating from an increase of the energy of the phonons of the $^1A_1$ state compared with those of the $^3A_2$ state. Previous work suggested that such an increase of phonon energies might be caused by the contribution of the double excitation configurations $|a_1\bar{a}_1\rangle$ in the wavefunction of the $^1A_1$ state[41]. However, our work suggests that the non-adiabatic coupling of the $^1A_1$ and ^1E singlet states is more likely responsible for the increase in phonon energies. A detailed comparison of the phonon modes of the $^1A_1$ and $^3A_2$ states can be found in Supplementary Note 6.

DISCUSSION

In summary, we studied the many-body electronic states of the NV^- center in diamond, including singlet states, using first-principles calculations based on TDDFT with semi-local and hybrid functionals and we computed vibrationally resolved optical spectra. We showed that TDDFT with analytical forces can be successfully applied to predict optical spectra of spin defects in solids, providing a robust description of both the electronic structure and atomic geometries of the many-body electronic states. In particular, TDDFT predicts the same energy ordering as experiments and the correct characteristics of the many-body electronic states, similar to those obtained using higher level methods, although the neglect of double excitations results in a slight overestimate of excitation energies relative to experiments. The computed vibrationally resolved absorption spectrum of the $^1E \rightarrow ^1A_1$ transition is in very good agreement with the experiment, thanks to an improved description of the atomic geometries and phonons of the singlet states obtained in our work. Our results show the key role played by non-adiabatic coupling in determining optical transitions. For example, we found that the equilibrium geometry of the $^1A_1$ state is similar to that of the $^3A_2$ ground state; however, the e type phonons of the former have significant higher energy than those of the ground state, due to the non-adiabatic coupling of the former with the ^1E states. Such coupling is also responsible for the anharmonicity of the $^1A_1$ state PES, which should be taken into account in obtaining absorption spectra in quantitative agreement with experiment. Interestingly, solving the effective Hamiltonian for the non-adiabatic coupling yields optically forbidden $\widetilde{A}_1$ and optically allowed $\widetilde{E}$ vibronic levels above the $^1\widetilde{E}$ ground vibronic state, consistent with PL measurements. Our study provides first principles predictions of the basic properties of the NV^- center in diamond, which are important for a comprehensive understanding of the optical spin-polarization cycle of this defect, and hence of its functionalities for quantum technology applications. In particular, the techniques presented here enable the modeling, from first principles, of the phonon side band of the optical absorption process between singlet states, which has been used for infrared-absorption-based magnetometry. The strategy applied here to the NV^- center in diamond is general and paves the way to the study of shelving states and optical spectra in other spin defects and materials.

METHODS

Electronic structure calculations

The ground state electronic structure of the NV^- center in diamond was obtained using DFT and the planewave pseudopotential method, as implemented in the Quantum Espresso package[57–59]. We used SG15 ONCV norm-conserving pseudopotentials[60,61] and the semi-local functional by Perdew, Burke, and Ernzerhof (PBE)[37] and the dielectric-dependent hybrid (DDH) functional[38]. The fraction of exact exchange used in the DDH functional is the inverse of the macroscopic dielectric constant of the system as reported in refs. [38,62]. The planewave energy cutoff was set to 85 Ry when using the PBE functional, and to 60 Ry for the DDH functional. We used a $(3 \times 3 \times 3)$ supercell containing 216 atomic sites for the NV^- center in diamond, with the lattice constant optimized for each functional[20]. The convergence of our results for VEEs with respect to the supercell size is reported in Supplementary Note 1. The Brillouin zone of the supercell was sampled with the Γ point.

Excited states were computed using the TDDFT method within the Tamm-Dancoff approximation. We obtained the energies and eigenvectors of low-lying excited states by iterative diagonalization of the linearized Liouville operator, as implemented in the WEST code[36,63]. An approximated non-collinear kernel was included in the spin-flip TDDFT calculations[30–32]. Analytical forces on nuclei in TDDFT were evaluated using the Lagrangian formulation by Hütter[39]. The equilibrium atomic geometries of excited states were obtained by minimizing the nuclear forces below the threshold of 0.01 eV/Å.

Phonon calculations

Phonon modes of the NV^- center were computed using the frozen phonon approach, with configurations generated with the PHONOPY package[64] and a displacement of 0.01 Å from equilibrium geometries of the $^3A_2$ and $^1A_1$ states, respectively. To compute the phonon modes of the $^3A_2$ state, DFT self-consistent calculations were conducted at displaced configurations. As for the phonon modes of the $^1A_1$ state, a DFT self-consistent calculation and an additional TDDFT excited state calculation were performed at each displaced configuration. Phonon calculations were performed only with the PBE functional due to the high computational cost of hybrid-DFT calculations. We estimated hybrid-DFT phonons by using a scaling factor[20]. Phonon modes are extrapolated to the dilute limit, approximated by a $(12 \times 12 \times 12)$ supercell cell with 13,824 atomic sites, using the force constant matrix embedding approach proposed by Alkauskas et al.[17,19].

Huang–Rhys factors and spectral functions

We write the absorption line shape as[65]

$$\sigma_{\mathrm{abs}}(\hbar\omega, T) \propto (\hbar\omega) A_{\mathrm{abs}}(\hbar\omega - E_{\mathrm{ZPL}}, T), \tag{4}$$

where E_{ZPL} is the energy of the zero-phonon line, and $\hbar\omega$ is the energy of the absorbed photon. T is the temperature. To be consistent with experiment[41], $T = 10$ K was used in the calculation of absorption line shape. The absorption spectral function is computed using the generating function approach[17,66,67]

$$A_{\mathrm{abs}}(\hbar\omega, T) = \frac{1}{2\pi}\int_{-\infty}^{\infty} \mathrm{e}^{\mathrm{i}\omega t} G_{\mathrm{abs}}(t, T) \mathrm{e}^{-\frac{\lambda|t|}{\hbar}} \mathrm{d}t, \tag{5}$$

where $\lambda = 0.1$ meV was used in our calculation to account for the broadening of the line shape. The generating function is written as

$$\begin{aligned} G_{\mathrm{abs}}(t, T) = \exp\Big[& \textstyle\int_{-\infty}^{\infty} S(\hbar\omega) e^{-\mathrm{i}\omega t} \mathrm{d}(\hbar\omega) - \sum_k S_k \\ & + \textstyle\int_{-\infty}^{\infty} C(\hbar\omega, T) e^{-\mathrm{i}\omega t} \mathrm{d}(\hbar\omega) \\ & + \textstyle\int_{-\infty}^{\infty} C(\hbar\omega, T) e^{\mathrm{i}\omega t} \mathrm{d}(\hbar\omega) - 2\sum_k \overline{n}_k(T) S_k \Big], \end{aligned} \tag{6}$$

where $\overline{n}_k(T)$ is the average occupation number of the kth phonon mode. $S(\hbar\omega)$ and $C(\hbar\omega, T)$ are the spectral densities of electron–phonon coupling,

$$S(\hbar\omega) = \sum_k S_k \delta(\hbar\omega - \hbar\omega_k), \quad C(\hbar\omega, T) = \sum_k \overline{n}_k(T) S_k \delta(\hbar\omega - \hbar\omega_k). \tag{7}$$

In actual calculations, the δ functions are replaced by Gaussian functions, and the broadening σ_k is varied linearly from 6 to 2 meV with the phonon energy, to account for the continuum of phonon modes participating in the optical transition. The HR factor S_k is computed as

$$S_k = \frac{\omega_k \Delta Q_k^2}{2\hbar}. \tag{8}$$

where ΔQ_k is the mass-weighted displacement along the kth mode, evaluated as

$$\Delta Q_k = \frac{1}{\omega_k^2} \sum_{\alpha=1}^{N} \sum_{i=x,y,z} \frac{\mathbf{F}_{\alpha i}}{\sqrt{M_\alpha}} \mathbf{e}_{k,\alpha i}. \tag{9}$$

Here M_α is the mass of the αth atom. For the $^1E \to {}^1A_1$ absorption, $\mathbf{F}$ represents the forces of the $^1A_1$ state evaluated at the equilibrium geometry of the ^1E state. ω_k ($\mathbf{e}_k$) is the frequency (eigenvector) of the kth phonon mode of the $^1A_1$ state.

Similarly, the PL line shape of the $^3A_2 \to {}^3E$ transition can be computed as[65]

$$I(\hbar\omega, T) \propto (\hbar\omega)^3 A_{\mathrm{emi}}(E_{\mathrm{ZPL}} - \hbar\omega, T). \tag{10}$$

Here the emission spectral function is calculated using the generating function built on HR factors computed with forces of the $^3A_2$ state, evaluated at the equilibrium structure of the ^3E state and with the phonons of the $^3A_2$ state. To be consistent with experiment[17], $T = 8$ K was used in the calculation of the PL line shape.

DATA AVAILABILITY

Data that support the findings of this study are available through the `Qresp`[68] curator at https://paperstack.uchicago.edu/paperdetails/6350c31b53d3f5972e8360bd?server=https://paperstack.uchicago.edu.

CODE AVAILABILITY

The TDDFT calculations and analytical nuclear forces are implemented in the open source code `WEST` (west-code.org/).

Received: 21 July 2022; Accepted: 1 November 2022;
Published online: 15 November 2022

REFERENCES

1. Wolfowicz, G. et al. Quantum guidelines for solid-state spin defects. *Nat. Rev. Mater.* **6**, 906–925 (2021).
2. Walker, J. Optical absorption and luminescence in diamond. *Rep. Prog. Phys.* **42**, 1605–1659 (1979).
3. Robledo, L., Bernien, H., Van Der Sar, T. & Hanson, R. Spin dynamics in the optical cycle of single nitrogen-vacancy centres in diamond. *N. J. Phys.* **13**, 025013 (2011).
4. Choi, S., Jain, M. & Louie, S. G. Mechanism for optical initialization of spin in NV^- center in diamond. *Phys. Rev. B* **86**, 041202 (2012).
5. Goldman, M. L. et al. State-selective intersystem crossing in nitrogen-vacancy centers. *Phys. Rev. B* **91**, 165201 (2015).
6. Thiering, G. & Gali, A. Theory of the optical spin-polarization loop of the nitrogen-vacancy center in diamond. *Phys. Rev. B* **98**, 085207 (2018).
7. Doherty, M. W. et al. The nitrogen-vacancy colour centre in diamond. *Phys. Rep.* **528**, 1–45 (2013).
8. Gali, A. Ab initio theory of the nitrogen-vacancy center in diamond. *Nanophotonics* **8**, 1907–1943 (2019).
9. Schirhagl, R., Chang, K., Loretz, M. & Degen, C. L. Nitrogen-vacancy centers in diamond: nanoscale sensors for physics and biology. *Annu. Rev. Phys. Chem.* **65**, 83–105 (2014).
10. Barry, J. F. et al. Sensitivity optimization for NV-diamond magnetometry. *Rev. Mod. Phys.* **92**, 015004 (2020).
11. Childress, L. & Hanson, R. Diamond NV centers for quantum computing and quantum networks. *MRS Bull.* **38**, 134–138 (2013).
12. Weber, J. et al. Quantum computing with defects. *Proc. Natl Acad. Sci. USA.* **107**, 8513–8518 (2010).
13. Waldherr, G. et al. Quantum error correction in a solid-state hybrid spin register. *Nature* **506**, 204–207 (2014).
14. Gali, A., Janzén, E., Deák, P., Kresse, G. & Kaxiras, E. Theory of spin-conserving excitation of the $N-V^-$ center in diamond. *Phys. Rev. Lett.* **103**, 186404 (2009).
15. Gali, A. Time-dependent density functional study on the excitation spectrum of point defects in semiconductors. *Phys. Status Solidi B* **248**, 1337–1346 (2011).
16. Thiering, G. & Gali, A. Ab initio calculation of spin-orbit coupling for an NV center in diamond exhibiting dynamic Jahn-Teller effect. *Phys. Rev. B* **96**, 081115 (2017).
17. Alkauskas, A., Buckley, B. B., Awschalom, D. D. & Van de Walle, C. G. First-principles theory of the luminescence lineshape for the triplet transition in diamond NV centres. *N. J. Phys.* **16**, 073026 (2014).
18. Ivády, V., Abrikosov, I. A. & Gali, A. First principles calculation of spin-related quantities for point defect qubit research. *npj Comput. Mater.* **4**, 1–13 (2018).
19. Razinkovas, L., Doherty, M. W., Manson, N. B., Van de Walle, C. G. & Alkauskas, A. Vibrational and vibronic structure of isolated point defects: The nitrogen-vacancy center in diamond. *Phys. Rev. B* **104**, 045303 (2021).
20. Jin, Y. et al. Photoluminescence spectra of point defects in semiconductors: Validation of first-principles calculations. *Phys. Rev. Mater.* **5**, 084603 (2021).
21. Ma, Y., Rohlfing, M. & Gali, A. Excited states of the negatively charged nitrogen-vacancy color center in diamond. *Phys. Rev. B* **81**, 041204 (2010).
22. Bhandari, C., Wysocki, A. L., Economou, S. E., Dev, P. & Park, K. Multiconfigurational study of the negatively charged nitrogen-vacancy center in diamond. *Phys. Rev. B* **103**, 014115 (2021).
23. Bockstedte, M., Schütz, F., Garratt, T., Ivády, V. & Gali, A. Ab initio description of highly correlated states in defects for realizing quantum bits. *npj Quantum Mater.* **3**, 1–6 (2018).
24. Ma, H., Govoni, M. & Galli, G. Quantum simulations of materials on near-term quantum computers. *npj Comput. Mater.* **6**, 85 (2020).
25. Ma, H., Sheng, N., Govoni, M. & Galli, G. First-principles studies of strongly correlated states in defect spin qubits in diamond. *Phys. Chem. Chem. Phys.* **22**, 25522–25527 (2020).
26. Ma, H., Sheng, N., Govoni, M. & Galli, G. Quantum embedding theory for strongly correlated states in materials. *J. Chem. Theory Comput.* **17**, 2116–2125 (2021).
27. Vorwerk, C., Sheng, N., Govoni, M., Huang, B. & Galli, G. Quantum embedding theories to simulate condensed systems on quantum computers. *Nat. Comput. Sci.* **2**, 424–432 (2022).
28. Huang, B., Govoni, M. & Galli, G. Simulating the electronic structure of spin defects on quantum computers. *PRX Quantum* **3**, 010339 (2022).
29. Sheng, N., Vorwerk, C., Govoni, M. & Galli, G. Green's function formulation of quantum defect embedding theory. *J. Chem. Theory Comput.* **18**, 3512–3522 (2022).
30. Wang, F. & Ziegler, T. Time-dependent density functional theory based on a noncollinear formulation of the exchange-correlation potential. *J. Chem. Phys.* **121**, 12191–12196 (2004).
31. Wang, F. & Ziegler, T. The performance of time-dependent density functional theory based on a noncollinear exchange-correlation potential in the calculations of excitation energies. *J. Chem. Phys.* **122**, 074109 (2005).
32. Li, Z. & Liu, W. Theoretical and numerical assessments of spin-flip time-dependent density functional theory. *J. Chem. Phys.* **136**, 024107 (2012).
33. Bernard, Y. A., Shao, Y. & Krylov, A. I. General formulation of spin-flip time-dependent density functional theory using non-collinear kernels: theory, implementation, and benchmarks. *J. Chem. Phys.* **136**, 204103 (2012).
34. Casanova, D. & Krylov, A. I. Spin-flip methods in quantum chemistry. *Phys. Chem. Chem. Phys.* **22**, 4326–4342 (2020).
35. Walker, B., Saitta, A. M., Gebauer, R. & Baroni, S. Efficient approach to time-dependent density-functional perturbation theory for optical spectroscopy. *Phys. Rev. Lett.* **96**, 113001 (2006).
36. Nguyen, N. L., Ma, H., Govoni, M., Gygi, F. & Galli, G. Finite-field approach to solving the Bethe-Salpeter equation. *Phys. Rev. Lett.* **122**, 237402 (2019).
37. Perdew, J. P., Burke, K. & Ernzerhof, M. Generalized gradient approximation made simple. *Phys. Rev. Lett.* **77**, 3865–3868 (1996).
38. Skone, J. H., Govoni, M. & Galli, G. Self-consistent hybrid functional for condensed systems. *Phys. Rev. B* **89**, 195112 (2014).
39. Hutter, J. Excited state nuclear forces from the Tamm–Dancoff approximation to time-dependent density functional theory within the plane wave basis set framework. *J. Chem. Phys.* **118**, 3928–3934 (2003).
40. Seth, M., Mazur, G. & Ziegler, T. Time-dependent density functional theory gradients in the Amsterdam density functional package: geometry optimizations of spin-flip excitations. *Theor. Chem. Acc.* **129**, 331–342 (2011).
41. Kehayias, P. et al. Infrared absorption band and vibronic structure of the nitrogen-vacancy center in diamond. *Phys. Rev. B* **88**, 165202 (2013).
42. Huang, K., Rhys, A. & Mott, N. F. Theory of light absorption and non-radiative transitions in *F*-centres. *Proc. R. Soc. Lond. Ser. A* **204**, 406–423 (1950).
43. Dumeige, Y. et al. Magnetometry with nitrogen-vacancy ensembles in diamond based on infrared absorption in a doubly resonant optical cavity. *Phys. Rev. B* **87**, 155202 (2013).
44. Jensen, K. et al. Cavity-enhanced room-temperature magnetometry using absorption by nitrogen-vacancy centers in diamond. *Phys. Rev. Lett.* **112**, 160802 (2014).
45. Wickenbrock, A. et al. Microwave-free magnetometry with nitrogen-vacancy centers in diamond. *Appl. Phys. Lett.* **109**, 053505 (2016).
46. Chatzidrosos, G. et al. Miniature cavity-enhanced diamond magnetometer. *Phys. Rev. Appl.* **8**, 044019 (2017).
47. Doherty, M. W., Manson, N. B., Delaney, P. & Hollenberg, L. C. The negatively charged nitrogen-vacancy centre in diamond: the electronic solution. *N. J. Phys.* **13**, 025019 (2011).
48. Maze, J. R. et al. Properties of nitrogen-vacancy centers in diamond: the group theoretic approach. *N. J. Phys.* **13**, 025025 (2011).
49. Davies, G. & Hamer, M. Optical studies of the 1.945 eV vibronic band in diamond. *Proc. R. Soc. Lond. A* **348**, 285–298 (1976).
50. Rogers, L. J., Armstrong, S., Sellars, M. J. & Manson, N. B. Infrared emission of the NV centre in diamond: Zeeman and uniaxial stress studies. *N. J. Phys.* **10**, 103024 (2008).
51. Goldman, M. L. et al. Phonon-induced population dynamics and intersystem crossing in nitrogen-vacancy centers. *Phys. Rev. Lett.* **114**, 145502 (2015).
52. Goldman, M. L. et al. Erratum: State-selective intersystem crossing in nitrogen-vacancy centers [Phys. Rev. B 91, 165201 (2015)]. *Phys. Rev. B* **96**, 039905 (2017).
53. Bersuker, I. *The Jahn-Teller Effect* (Cambridge University Press, 2006).
54. Manson, N., Rogers, L., Doherty, M. & Hollenberg, L. Optically induced spin polarisation of the NV-centre in diamond: role of electron-vibration interaction. Preprint at https://arxiv.org/abs/1011.2840 (2010).
55. Rogers, L. J. et al. Singlet levels of the NV^- centre in diamond. *N. J. Phys.* **17**, 013048 (2015).
56. Acosta, V., Jarmola, A., Bauch, E. & Budker, D. Optical properties of the nitrogen-vacancy singlet levels in diamond. *Phys. Rev. B* **82**, 201202 (2010).
57. Giannozzi, P. et al. Quantum espresso: a modular and open-source software project for quantum simulations of materials. *J. Phys. Condens. Matter* **21**, 395502 (2009).
58. Giannozzi, P. et al. Advanced capabilities for materials modelling with quantum espresso. *J. Phys. Condens. Matter* **29**, 465901 (2017).
59. Giannozzi, P. et al. Quantum espresso toward the exascale. *J. Chem. Phys.* **152**, 154105 (2020).

60. Hamann, D. R. Optimized norm-conserving vanderbilt pseudopotentials. *Phys. Rev. B* **88**, 085117 (2013).
61. Schlipf, M. & Gygi, F. Optimization algorithm for the generation of ONCV pseudopotentials. *Comput. Phys. Commun.* **196**, 36–44 (2015).
62. Seo, H., Ma, H., Govoni, M. & Galli, G. Designing defect-based qubit candidates in wide-gap binary semiconductors for solid-state quantum technologies. *Phys. Rev. Mater.* **1**, 075002 (2017).
63. Govoni, M. & Galli, G. Large scale GW calculations. *J. Chem. Theory Comput.* **11**, 2680–2696 (2015).
64. Togo, A. & Tanaka, I. First principles phonon calculations in materials science. *Scr. Mater.* **108**, 1–5 (2015).
65. Razinkovas, L., Maciaszek, M., Reinhard, F., Doherty, M. W. & Alkauskas, A. Photoionization of negatively charged NV centers in diamond: theory and ab initio calculations. *Phys. Rev. B* **104**, 235301 (2021).
66. Kubo, R. & Toyozawa, Y. Application of the method of generating function to radiative and non-radiative transitions of a trapped electron in a crystal. *Prog. Theor. Phys.* **13**, 160–182 (1955).
67. Lax, M. The Franck-Condon principle and its application to crystals. *J. Chem. Phys.* **20**, 1752–1760 (1952).
68. Govoni, M. et al. Qresp, a tool for curating, discovering and exploring reproducible scientific papers. *Sci. Data* **6**, 1–7 (2019).

ACKNOWLEDGEMENTS

We thank Dr. He Ma, Nan Sheng and Dr. Christian Vorwerk for fruitful discussions. This work was supported by the computational materials science center Midwest Integrated Center for Computational Materials (MICCoM) for the implementation of spin-flip time-dependent density functional theory in WEST, and by AFOSR Grant No. FA9550-19-1-0358 for the application of the code to study absorption spectra in diamond. MICCoM is part of the Computational Materials Sciences Program funded by the U.S. Department of Energy, Office of Science, Basic Energy Sciences, Materials Sciences, and Engineering Division through the Argonne National Laboratory, under Contract No. DE-AC02-06CH11357. This research used resources of the National Energy Research Scientific Computing Center (NERSC), a DOE Office of Science User Facility supported by the Office of Science of the U.S. Department of Energy under Contract No. DE-AC02-05CH11231, and resources of the University of Chicago Research Computing Center.

AUTHOR CONTRIBUTIONS

Y.J., M.G., and G.G. designed the research. Y.J. implemented the time-dependent density functional theory and analytical nuclear forces and performed calculations, with supervision by M.G. and G.G. All authors wrote the manuscript.

COMPETING INTERESTS

The authors declare no competing interests.

ADDITIONAL INFORMATION

Supplementary information The online version contains supplementary material available at https://doi.org/10.1038/s41524-022-00928-y.

Correspondence and requests for materials should be addressed to Marco Govoni or Giulia Galli.